

This work has been submitted to the IEEE for possible publication. Copyright may be transferred without notice, after which this version may no longer be accessible.

arXiv:2410.01057v1 [eess.SY] 1 Oct 2024

Uncertainty Modelling and Robust Observer Synthesis using the Koopman Operator

Steven Dahdah, *Student Member, IEEE*, James Richard Forbes, *Member, IEEE*

Abstract—This paper proposes a robust nonlinear observer synthesis method for a population of systems modelled using the Koopman operator. The Koopman operator allows nonlinear systems to be rewritten as infinite-dimensional linear systems. A finite-dimensional approximation of the Koopman operator can be identified directly from data, yielding an approximately linear model of a nonlinear system. The proposed observer synthesis method is made possible by this linearity that in turn allows uncertainty within a population of Koopman models to be quantified in the frequency domain. Using this uncertainty model, linear robust control techniques are used to synthesize robust nonlinear Koopman observers. A population of several dozen motor drives is used to experimentally demonstrate the proposed method. Manufacturing variation is characterized in the frequency domain, and a robust Koopman observer is synthesized using mixed \mathcal{H}_2 - \mathcal{H}_∞ optimal control.

Index Terms—Observer design, state estimation, robust control, Koopman operator theory, nonlinear systems, uncertainty quantification, system identification, manufacturing variation, linear matrix inequalities (LMIs), motor drives.

I. INTRODUCTION

THE design of controllers and observers that are robust to plant uncertainty or variation is a challenging engineering problem, particularly when the plant is nonlinear. A robust controller or observer provides performance guarantees when deployed on any plant within a specified uncertainty set. This uncertainty set could represent a population of nominally identical systems with some variability, such as a product subject to manufacturing variation, but it could also represent the effect of modelling error or neglected dynamics for a single system. By explicitly considering uncertainty in the design process, robust controllers and observers can improve yield, reliability, and safety in real-world scenarios.

Robust control theory, which can be used to synthesize either controllers or observers, is well-developed but generally limited to linear plants [1]–[3]. In this framework, nonlinear effects are typically treated as perturbations to a linear nominal plant [3, §9.1]. One approach to extending robust control theory to nonlinear plants involves the Koopman operator [4]–[7], a tool that allows nonlinear systems to be represented globally by infinite-dimensional linear systems. This is achieved by

viewing their dynamics in terms of a set of nonlinear lifting functions whose time evolution is governed by the Koopman operator. Finite-dimensional approximations of the Koopman operator can be identified from data and used in the robust control framework with little modification.

In this paper, a robust nonlinear observer design methodology based on a population of approximate Koopman models identified using input-output data is presented. Then, an industrially relevant nonlinear observer synthesis example is discussed, where experimental data from a batch of 38 motor drives with Harmonic Drive gearboxes is used to demonstrate the proposed method. Harmonic Drive gearboxes are common in aerospace, robotics, and industry due to their compact form factor, high reduction ratio, and lack of backlash [8], [9]. However, these gearboxes are affected by nonlinear oscillations that can degrade tracking performance and excite vibration modes in the systems where they are used [8], [9]. Motor drives with Harmonic Drive gearboxes therefore require nonlinear nominal models to synthesize a robust observer that can predict this behaviour.

A. Related work

Observer synthesis methods for specific types of uncertain nonlinear systems have previously been presented in the literature. Gain-scheduled linear observers are designed in [10]–[12] for linear and bilinear parameter varying systems. \mathcal{H}_∞ optimal observers for systems with Lipschitz nonlinearities are synthesized in [13]–[16]. A sliding-mode \mathcal{H}_∞ optimal observer for Lipschitz nonlinear systems is proposed in [17].

Early work using the Koopman operator for state estimation introduces the Koopman observer form (KOF), a particular state-space form computed from the estimated eigendecomposition of the Koopman operator [18], [19]. The KOF is used in [20] to design a Koopman Kalman filter to estimate the flow field near an actuated airfoil from pressure measurements. A generalized maximum likelihood variant of the Koopman Kalman filter is introduced in [21], where it is used to estimate the rotor angle and speed of a series of synchronous generators. In [22], a Koopman Luenberger observer is designed to detect faulty actuators in a multirotor system. Koopman observer design for models with bilinear lifting functions is considered in [23]. Koopman state estimation in a batch optimization framework is discussed in [24], [25], while simultaneous localization and mapping (SLAM) is additionally considered in [25].

To date, robust observer synthesis with the Koopman operator has not been considered, but robust linear time-invariant

This work is supported by the Natural Sciences and Engineering Research Council of Canada (NSERC) Discovery Grants program, the *Fonds de recherche en santé — Nature et technologies* (FRQNT), the *Institut de valorisation des données* (IVADO), the Canadian Institute for Advanced Research (CIFAR), and the *Centre de recherches mathématiques* (CRM), as well as by Mecaademic through the Mitacs Accelerate program.

S. Dahdah and J. R. Forbes are with the Department of Mechanical Engineering, McGill University, Montreal QC H3A 0C3, Canada (e-mail: steven.dahdah@mail.mcgill.ca; james.richard.forbes@mcgill.ca).

(LTI) controller synthesis using the Koopman operator has been addressed in [26]–[30]. In [26], \mathcal{H}_2 optimal control is used to synthesize controllers that perform robustly in the face of uncertainty modelled by polytope sets of Koopman models. The uncertainty is due to the use of multiple datasets to identify multiple Koopman models of the same system. The synthesized controllers are tested in simulation using a Duffing oscillator system and the Kroteweg–De Vries partial differential equation. Uncertainty due to the finite-dimensional approximation of an infinite-dimensional Koopman operator is represented in [27], [28]. Controllers are designed to guarantee stability in the largest possible regions of attraction and are tested on simulated Van der Pol oscillator [27] and inverted pendulum [28] systems. Biased Koopman models identified from noisy data are considered in [29], where uncertainty is modelled based on a known sector bounded model mismatch. A dual-loop \mathcal{H}_∞ control approach is used to attain both robust stability and robust performance guarantees. The approach is demonstrated using a simulated Van der Pol oscillator. In [30], robust \mathcal{H}_∞ control is applied to a linear parameter-varying Koopman representation. Uncertainty due to the linear parameter-varying nature of the model, along with known model approximation error, is modelled in the frequency domain. The uncertainty is bounded using constant weighting functions in an additive uncertainty representation. A mixed \mathcal{H}_2 - \mathcal{H}_∞ control problem is solved to guarantee the robust stability of the Koopman controller. The performance of the synthesized controller is demonstrated on a simulated bilinear motor model. While robustness is not considered in [31], a sophisticated \mathcal{H}_∞ design procedure with dynamic performance weighting functions is outlined in the lifted space. The synthesized \mathcal{H}_∞ controller is demonstrated on simulated Van der Pol oscillator and two-mass-Duffing-spring systems. So far, no Koopman control approaches have been demonstrated outside of simulation, and no Koopman uncertainty models have characterized variation within a population of nominally identical plants subject to individual variation.

For the sake of completeness, note that comprehensive reviews of Koopman control approaches based on the linear-quadratic regulator (LQR) and model predictive control (MPC) can be found in [7], [32], [33]. Koopman-based MPC algorithms that consider other definitions of robustness include [34]–[37].

B. Contribution

The key methodological contributions of this paper are

- 1) the frequency-domain quantification of uncertainty in a population of Koopman models, and
- 2) a robust nonlinear observer synthesis approach for a population of Koopman models.

Furthermore, this work extends the input-output observer framework of [11], [38], by introducing mixed \mathcal{H}_2 - \mathcal{H}_∞ optimal control and non-additive uncertainty forms to the method.

The proposed observer synthesis method is demonstrated experimentally on a population of motor drives, leading to the following technological contributions.

- 1) The creation of a publicly available dataset consisting of trajectories from 38 individual motor drives in loaded and unloaded conditions [39].
- 2) The development of physics-inspired Koopman lifting functions for motor drives with Harmonic Drive gearboxes.
- 3) The evaluation of multiple different uncertainty forms for each choice of nominal plant model for a population of Koopman models.
- 4) The use of nontrivial weighting functions to bound residuals for a population of Koopman models.
- 5) The experimental, rather than simulated, validation of a robust nonlinear observer based on mixed \mathcal{H}_2 - \mathcal{H}_∞ optimal control.

Two additional minor contributions are discussed in the Appendices. The first is an outlier detection approach for incorrectly-installed motor drives using the frequency-domain uncertainty model, and the second is a phase offset calibration procedure for Harmonic Drive gearbox oscillations.

The aforementioned methodological contributions are general, and can be applied to a wide range of systems, while the technological contributions are related to specific challenges posed by the motor drive system under consideration.

C. Outline

The remainder of this paper is structured as follows. Section II summarizes robust control theory, its applications to robust observer synthesis, and Koopman operator theory. Section III describes the proposed robust nonlinear observer synthesis methodology. Section IV presents experimental validation of the methodology using a dataset of 38 nonlinear motor drives. Finally, Section V concludes the paper.

Appendix A discusses how frequency-domain uncertainty modelling can be used to detect outlier motor drives, and Appendix B presents a phase offset calibration procedure for motor drives with Harmonic Drive gearbox oscillations.

II. BACKGROUND

A. Robust control theory

This section outlines the robust control fundamentals required to quantify uncertainty within a population of LTI systems and synthesize a robust controller or observer using that uncertainty model.

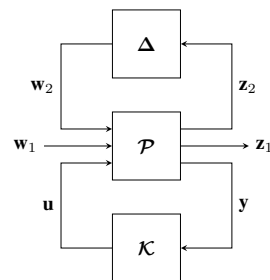


Fig. 1: The generalized plant \mathcal{P} for the robust optimal control problem in feedback with a controller \mathcal{K} and an uncertainty block Δ .

1) *Notation:* Let $\mathbf{y} : \mathbb{Z}_{\geq 0} \rightarrow \mathbb{R}^{n \times 1}$ denote a discrete-time signal whose value at time k is \mathbf{y}_k [40, §1.2]. A time-invariant system is a mapping from signals to signals, denoted $\mathcal{G} : \ell_{2e} \rightarrow \ell_{2e}$, where ℓ_{2e} is the extended inner product sequence space [2, §B.1.1]. For LTI systems, \mathcal{G} is a linear operator. A minimal state-space realization of an LTI system is denoted [2, §3.2.1]

$$\mathcal{G} \overset{\text{min}}{\sim} \left[\begin{array}{c|c} \mathbf{A} & \mathbf{B} \\ \hline \mathbf{C} & \mathbf{D} \end{array} \right]. \quad (1)$$

Another way to realize an LTI system is through its transfer matrix,

$$\mathbf{y}(z) = \mathbf{G}(z)\mathbf{u}(z), \quad (2)$$

where $\mathbf{y}(z)$, $z \in \mathbb{C}$ denotes the z -transform of a signal [41, §3.5.2]. Evaluating the transfer matrix at $z = e^{j\theta}$, where $\theta = 2\pi\Delta t f$ is the discrete-time frequency, Δt is the sampling period, and f is the continuous-time frequency, yields the frequency response of the system.

2) *Norms of systems:* The size of a system can be quantified with a norm. The \mathcal{H}_∞ norm of a system \mathcal{G} is the worst-case gain from $\|\mathbf{u}\|_2$ to $\|\mathbf{y}\|_2 = \|\mathcal{G}\mathbf{u}\|_2$. That is [2, §B.1.1],

$$\|\mathcal{G}\|_\infty = \sup_{\mathbf{u} \in \ell_2, \mathbf{u} \neq \mathbf{0}} \frac{\|\mathcal{G}\mathbf{u}\|_2}{\|\mathbf{u}\|_2}. \quad (3)$$

In the frequency domain, this definition is equivalent to [2, §B.1.1]

$$\|\mathcal{G}\|_\infty = \sup_{\theta \in (-\pi, \pi]} \bar{\sigma}(\mathbf{G}(e^{j\theta})), \quad (4)$$

where $\bar{\sigma}(\cdot)$ denotes the maximum singular value of a matrix. The \mathcal{H}_∞ norm of a system can be viewed as the peak magnitude of its frequency response.

The \mathcal{H}_2 norm is

$$\|\mathcal{G}\|_2 = \sqrt{\frac{1}{2\pi} \int_{-\pi}^{\pi} \text{tr}(\mathbf{G}(e^{j\theta})^H \mathbf{G}(e^{j\theta})) d\theta}, \quad (5)$$

where $\mathbf{G}(e^{j\theta})$ is the transfer matrix representation of \mathcal{G} [42, §4.4] [43]. The \mathcal{H}_2 norm can be viewed as the expected root-mean-squared (RMS) output of a system when the input is unit variance white noise [2, §3.3.3] [3, §5.7] [43].

3) *Optimal controller synthesis:* The generalized plant, \mathcal{P} , depicted in Figure 1, is central to the robust control problem [1, §3.8]. It consists of an interconnection of the system to be controlled with a series of weighting functions used to specify performance requirements. The controller inputs and outputs, \mathbf{u} and \mathbf{y} , represent the signals accessible to a controller \mathcal{K} . The performance inputs and outputs, \mathbf{w}_1 and \mathbf{z}_1 , encode performance requirements to be optimized. Performance inputs could include disturbance and reference signals, while performance outputs could include control effort and tracking error. The uncertainty inputs and outputs, \mathbf{w}_2 and \mathbf{z}_2 , connect the generalized plant to the uncertainty block, Δ , which can be any system satisfying $\|\Delta\|_\infty \leq 1$.

In the absence of uncertainty, an optimal controller minimizes the impact of \mathbf{w}_1 on $\mathbf{z}_1 = \mathcal{T}_{11}\mathbf{w}_1$. That is, it solves

$$\min_{\mathcal{K}} \|\mathcal{T}_{11}\| \quad (6)$$

for some system norm of \mathcal{T}_{11} , like the \mathcal{H}_∞ norm or the \mathcal{H}_2 norm. Weighting functions included inside the generalized plant allow performance metrics, like disturbance rejection or tracking error, to be targeted over a particular frequency band. Posing an optimal control problem in this manner guarantees the asymptotic stability of the closed-loop system as long as a system norm of \mathcal{T}_{11} is finite [3].

Now consider the case where model uncertainty is present. Let $\mathbf{z}_2 = \mathcal{T}_{22}\mathbf{w}_2$. Assuming that \mathcal{K} asymptotically stabilizes \mathcal{P} for $\Delta = \mathbf{0}$, the small-gain theorem [1, §4.9.4] implies that the closed-loop system in Figure 1 is asymptotically stable for any $\|\Delta\|_\infty \leq 1$ if $\|\mathcal{T}_{22}\|_\infty < 1$. This property is called *robust stability*. The mixed \mathcal{H}_2 - \mathcal{H}_∞ optimal controller achieves robust stability by solving [44].

$$\min_{\mathcal{K}} \|\mathcal{T}_{11}\|_2 \quad (7)$$

$$\text{s.t. } \|\mathcal{T}_{22}\|_\infty < 1. \quad (8)$$

Let $[\mathbf{z}_1^T \ \mathbf{z}_2^T]^T = \mathcal{T}[\mathbf{w}_1^T \ \mathbf{w}_2^T]^T$. The \mathcal{H}_∞ optimal controller also achieves robust stability by solving [1, §9.3]

$$\gamma = \arg \min_{\mathcal{K}} \|\mathcal{T}\|_\infty, \quad (9)$$

and verifying that $\gamma < 1$.

4) *Quantifying uncertainty:* To model the uncertainty for a given population of systems, an uncertainty structure must be chosen and an uncertainty weighting function must be found. Consider a nominal plant $\mathbf{G}(z)$, a perturbed plant $\mathbf{G}_p(z)$, and a perturbation, or residual, $\mathbf{E}(z)$. The perturbation can be expressed as [1, §8.2.3]

$$\mathbf{E}(z) = \mathbf{W}_2(z)\Delta(z)\mathbf{W}_1(z), \quad \|\Delta(z)\|_\infty \leq 1, \quad (10)$$

where often one of the weighting functions is set to identity. These weights are placed inside the generalized plant, such that the input of $\mathbf{W}_1(z)$ is \mathbf{w}_2 and the output of $\mathbf{W}_2(z)$ is \mathbf{z}_2 . The additive uncertainty model corresponds to [1, §8.2.3]

$$\mathbf{G}_p(z) = \mathbf{G}(z) + \mathbf{E}_a(z). \quad (11)$$

Let $\mathbf{W}_2(z) = \mathbf{1}$. The remaining weighting function $\mathbf{W}_1(z)$ is designed to satisfy [1, §8.2.3]

$$\|\mathbf{G}_p(z) - \mathbf{G}(z)\|_\infty \leq \|\Delta(z)\|_\infty \|\mathbf{W}_1(z)\|_\infty \leq \|\mathbf{W}_1(z)\|_\infty \quad (12)$$

for all perturbed plants. Other common uncertainty forms are [1, §8.2.3]

- input multiplicative, $\mathbf{G}_p(z) = \mathbf{G}(z)(\mathbf{1} + \mathbf{E}_i(z))$,
- output multiplicative, $\mathbf{G}_p(z) = (\mathbf{1} + \mathbf{E}_o(z))\mathbf{G}(z)$,
- inverse additive, $\mathbf{G}_p(z) = \mathbf{G}(z)(\mathbf{1} - \mathbf{E}_{ia}(z)\mathbf{G}(z))^{-1}$,
- inverse input mult., $\mathbf{G}_p(z) = \mathbf{G}(z)(\mathbf{1} - \mathbf{E}_{ii}(z))^{-1}$, and
- inverse output mult., $\mathbf{G}_p(z) = (\mathbf{1} - \mathbf{E}_{io}(z))^{-1}\mathbf{G}(z)$.

Given a population of perturbed plants, each perturbation $\mathbf{E}(z)$ is typically calculated frequency-by-frequency. An uncertainty weight $\mathbf{W}(z)$ that bounds all the perturbations is then designed and incorporated into the generalized plant.

B. Robust observer design

Optimal observer design can be viewed as optimal controller design with a particular choice of generalized plant. This section provides a brief overview of linear observers and their relationship to linear controllers. Consider the state-space representation of a strictly proper LTI system,

$$\mathbf{x}_{k+1} = \mathbf{A}\mathbf{x}_k + \mathbf{B}\mathbf{u}_k, \quad (13)$$

$$\mathbf{y}_k = \mathbf{C}\mathbf{x}_k, \quad (14)$$

where (\mathbf{A}, \mathbf{C}) is observable. The structure of the most common type of observer, the *Luenberger observer*, is [11]

$$\hat{\mathbf{x}}_{k+1} = \mathbf{A}\hat{\mathbf{x}}_k + \mathbf{B}\mathbf{u}_k + \mathbf{L}(\mathbf{y}_k - \hat{\mathbf{y}}_k), \quad (15)$$

$$\hat{\mathbf{y}}_k = \mathbf{C}\hat{\mathbf{x}}_k, \quad (16)$$

where \mathbf{L} is the observer gain. The observer gain is chosen to asymptotically stabilize the error dynamics [11]

$$\mathbf{e}_{k+1} = (\mathbf{A} - \mathbf{L}\mathbf{C})\mathbf{e}_k, \quad (17)$$

where $\mathbf{e}_k = \hat{\mathbf{x}}_k - \mathbf{x}_k$.

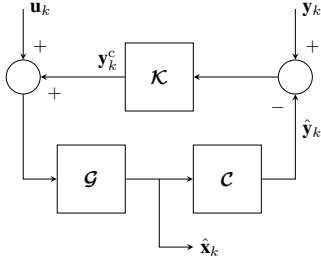


Fig. 2: The structure of an input-output observer. Note that the output matrix \mathbf{C} is drawn as a separate system from \mathcal{G} to allow access to the state estimate $\hat{\mathbf{x}}_k$.

However, observers need not be limited to static gains. In [11], [38], robust optimal control techniques are used to synthesize *input-output observers* of the form

$$\mathbf{x}_{k+1}^c = \mathbf{A}^c \mathbf{x}_k^c + \mathbf{B}^c (\mathbf{y}_k - \hat{\mathbf{y}}_k), \quad (18)$$

$$\mathbf{y}_k^c = \mathbf{C}^c \mathbf{x}_k^c + \mathbf{D}^c (\mathbf{y}_k - \hat{\mathbf{y}}_k), \quad (19)$$

$$\hat{\mathbf{x}}_{k+1} = \mathbf{A}\hat{\mathbf{x}}_k + \mathbf{B}(\mathbf{u}_k + \mathbf{y}_k^c), \quad (20)$$

$$\hat{\mathbf{y}}_k = \mathbf{C}\hat{\mathbf{x}}_k. \quad (21)$$

A block diagram of an input-output observer is shown in Figure 2, where

$$\mathcal{K} \stackrel{\min}{\sim} \left[\begin{array}{c|c} \mathbf{A}^c & \mathbf{B}^c \\ \hline \mathbf{C}^c & \mathbf{D}^c \end{array} \right], \quad \mathcal{C}\mathcal{G} \stackrel{\min}{\sim} \left[\begin{array}{c|c} \mathbf{A} & \mathbf{B} \\ \hline \mathbf{C} & \mathbf{0} \end{array} \right]. \quad (22)$$

Inside the observer, a copy of the nominal plant is used for comparison against measurements. The synthesized controller \mathcal{K} compares the measurements with the nominal plant's output and makes corrections to its input accordingly. Note that the output matrix \mathbf{C} is drawn as a separate system \mathcal{C} in Figure 2, to allow access to the state estimate $\hat{\mathbf{x}}_k$ in the block diagram. An example of a generalized plant for an input-output observer design problem can be found later in Figure 9.

Unlike a controller, an observer cannot destabilize the observed system. As such, robustness in an observer does not

refer to robust stability. Instead, as in [11], [38], robustness in an observer refers to insensitivity of performance to model uncertainty. Loosely, the uncertainty weight is therefore used to inform the observer of when it can trust the predictions of its internal nominal model. When uncertainty is high, the nominal model may not match the true system, so external measurements should be used to correct the model predictions. When uncertainty is low, the nominal model is likely to match the true systems, so noise and disturbances can be rejected by using the observer's internal model without correction.

C. Koopman operator theory

This section provides a brief overview of Koopman operator theory with exogenous inputs.

1) *The Koopman operator*: Consider the nonlinear difference equation

$$\mathbf{x}_{k+1} = \mathbf{f}(\mathbf{x}_k, \mathbf{u}_k), \quad (23)$$

where the state is $\mathbf{x}_k \in \mathcal{M} \subseteq \mathbb{R}^{m \times 1}$ and the input is $\mathbf{u}_k \in \mathcal{N} \subseteq \mathbb{R}^{n \times 1}$. Also consider the set \mathcal{H} of all scalar-valued *lifting functions*, $\psi : \mathcal{M} \times \mathcal{N} \rightarrow \mathbb{R}$. The *Koopman operator*, $\mathcal{U} : \mathcal{H} \rightarrow \mathcal{H}$, composes lifting functions with $\mathbf{f}(\cdot)$, advancing them in time by one timestep. That is,

$$(\mathcal{U}\psi)(\mathbf{x}_k, \mathbf{u}_k) = \psi(\mathbf{f}(\mathbf{x}_k, \mathbf{u}_k), \star), \quad (24)$$

where $\star = \mathbf{u}_k$ if the input has state-dependent dynamics, or $\star = \mathbf{0}$ if the input has no dynamics [45, §6.5]. The set \mathcal{H} is often an infinite-dimensional Hilbert space. Sometimes this space is explicitly chosen, while other times, it is implicitly defined by the lifting functions [32, §2.1].

To approximate the Koopman operator in finite dimensions, a finite subset of lifting functions must be chosen. Let the *vector-valued lifting functions* $\psi : \mathcal{M} \times \mathcal{N} \rightarrow \mathbb{R}^{p \times 1}$ be written as

$$\psi(\mathbf{x}_k, \mathbf{u}_k) = \begin{bmatrix} \vartheta(\mathbf{x}_k) \\ \mathbf{v}(\mathbf{x}_k, \mathbf{u}_k) \end{bmatrix}, \quad (25)$$

where the state-dependent lifting functions are $\vartheta : \mathcal{M} \rightarrow \mathbb{R}^{p_\vartheta \times 1}$, the input-dependent lifting functions are $\mathbf{v} : \mathcal{M} \times \mathcal{N} \rightarrow \mathbb{R}^{p_v \times 1}$, and $p_\vartheta + p_v = p$. A finite-dimensional approximation of (24) is [45, §6.5.1]

$$\vartheta(\mathbf{x}_{k+1}) = \mathbf{U}\vartheta(\mathbf{x}_k, \mathbf{u}_k) + \epsilon_k, \quad (26)$$

where $\mathbf{U} = [\mathbf{A} \quad \mathbf{B}]$ is the *Koopman matrix*. Expanding (26) results in the linear state-space form,

$$\vartheta(\mathbf{x}_{k+1}) = \mathbf{A}\vartheta(\mathbf{x}_k) + \mathbf{B}\mathbf{v}(\mathbf{x}_k, \mathbf{u}_k) + \epsilon_k. \quad (27)$$

2) *Data-driven Koopman operator approximation*: To approximate the Koopman matrix from a dataset $\mathcal{D} = \{\mathbf{x}_k, \mathbf{u}_k\}_{k=0}^q$, lifting functions must first be chosen. Koopman lifting functions can be inspired by the dynamics of the system in question [46]–[48], taken from a standard set of basis functions like polynomials, sinusoids, or radial basis functions [49]–[53], or chosen to approximate a given kernel [24], [54], [55]. Time-delayed states are also often included in the lifted state [49], [56], [57].

For a given choice of lifting functions, consider the lifted snapshot matrices

$$\Psi = [\psi_0 \ \psi_1 \ \cdots \ \psi_{q-1}] \in \mathbb{R}^{p \times q}, \quad (28)$$

$$\Theta_+ = [\vartheta_1 \ \vartheta_2 \ \cdots \ \vartheta_q] \in \mathbb{R}^{p \vartheta \times q}, \quad (29)$$

where $\psi_k = \psi(\mathbf{x}_k, \mathbf{u}_k)$ and $\vartheta_k = \vartheta(\mathbf{x}_k)$.

Least-squares is the simplest way to approximate the Koopman matrix from data. Minimizing ϵ_k leads to the optimization problem

$$\min_{\mathbf{U}} \frac{1}{q} \|\Theta_+ - \mathbf{U}\Psi\|_F^2, \quad (30)$$

whose solution is [45, §1.2.1]

$$\mathbf{U} = \Theta_+ \Psi^\dagger. \quad (31)$$

Extended dynamic mode decomposition (EDMD) [58] improves performance and numerical conditioning in the least-squares problem when the dataset contains many fewer states than snapshots (*i.e.*, when $p \ll q$) [45, §10.3]. Assuming Ψ is full rank, the EDMD approximation of the Koopman matrix is

$$\mathbf{U} = \Theta_+ (\Psi^\top \Psi^{\top\dagger}) \Psi^\dagger = (\Theta_+ \Psi^\top) (\Psi \Psi^\top)^\dagger = \mathbf{G} \mathbf{H}^\dagger, \quad (32)$$

where

$$\mathbf{G} = \frac{1}{q} \Theta_+ \Psi^\top \in \mathbb{R}^{p \vartheta \times p}, \quad \mathbf{H} = \frac{1}{q} \Psi \Psi^\top \in \mathbb{R}^{p \times p}. \quad (33)$$

Note that, when the columns of Ψ are linearly independent, $\mathbf{H} = \mathbf{H}^\top > 0$.

III. METHODOLOGY

The proposed robust nonlinear observer synthesis method applies the input-output observer structure of [11], [38] to a population of Koopman models. The steps of the proposed method are as follows.

- 1) Identify a Koopman model for every plant in a population using the same set of lifting functions.
- 2) Select a nominal plant and an uncertainty form, compute residuals, and design an uncertainty weighting function to bound the residuals in the frequency domain.
- 3) Design performance weighting functions, form the generalized plant, and synthesize a robust controller (*e.g.*, \mathcal{H}_∞ , mixed \mathcal{H}_2 - \mathcal{H}_∞).
- 4) Interconnect the controller with the nominal Koopman plant as in Figure 2.

Thanks to the linearity of the Koopman operator, the input-output observer structure requires little modification, as the observer synthesis process takes place in the lifted space. This is viewed as a positive aspect of the approach, as existing robust control and estimation techniques are powerful and well-studied.

One key difference between the proposed Koopman observer and a linear observer is how the nominal model is used when the observer is deployed. During synthesis, the Koopman model is treated as an LTI system. However, during operation, the original system's state is retracted and re-lifted at each timestep. This prevents the system interconnection in Figure 2 from being collapsed into a single LTI block, but

yields more accurate model predictions, as it ensures that the structure of the lifted state is always respected. This approach results in the *local error* definition of [59]. Note that when comparing Koopman observers to their linear counterparts, weights on lifted states should be zero to ensure that both methods minimize the same cost functions.

IV. EXPERIMENTAL VALIDATION

In this section, the proposed robust nonlinear observer synthesis methodology is applied to a population of 38 motor drives. Each motor drive, pictured in Figure 3, consists of an electric motor and a Harmonic Drive gearbox. The gearbox introduces a periodic oscillation into the system which cannot be captured by a linear model [8], [9]. A Koopman model



Fig. 3: Motor drive used to generate the training data, which consists of a motor with a Harmonic Drive gearbox. The gearbox introduces nonlinear oscillations into the system, leading to tracking errors at specific frequencies related to the input velocity. Photo courtesy of Alexandre Coulombe.

for each drive is identified, manufacturing uncertainty is characterized in the frequency domain, and a robust Koopman observer is designed to estimate motor velocity and current using position measurements. Each motor drive is identified with and without an asymmetric inertial load. The models used for observer synthesis are identified using unloaded drives, so the motor current estimation errors can be treated as load torque estimates. The uncertainty characterization used for robust observer design can also be used to detect incorrectly installed motor drives. An outlier detection approach based on the uncertainty characterization done in this section is discussed in Appendix A.

The full motor drive dataset is available for download at [39]. A datasheet following the format of [60] is also provided. The software required to fully reproduce the results of this paper is available at https://github.com/decargroup/robust_observer_koopman. This code extends `pykoop` [61], the authors' open-source Koopman operator approximation library for Python.

A. Dataset

The motor drives under consideration operate in closed-loop, accepting position and velocity reference signals and returning position, velocity, and current measurements. The velocity measurements are computed from position measurements by the drives via a filtered finite difference scheme. The dataset consists of 40 episodes per drive, each approximately 20 s long. The drive is loaded with an asymmetric inertial load for half of the episodes. The loaded and unloaded datasets are split into 18 training episodes and two test episodes. The reference position, reference velocity, measured position, measured velocity, and measured motor current are recorded at 1 kHz. The positions and velocities are recorded in rad and rad/s respectively at the output shaft of the gearbox, while the current is recorded as a fraction of the drive's full-scale current. The gearboxes under consideration reduce input velocities by a factor of 100.

The drive's control software accepts position checkpoints and generates the smoothed trapezoidal velocity trajectories required to reach each checkpoint. Each episode contains 10 pseudorandom position checkpoints set within one revolution of the gearbox output shaft in either direction. The resulting velocity profile resembles a smoothed pseudorandom binary sequence (PRBS) [62, §13.3]. For all episodes, the maximum allowed velocity and acceleration settings are set in the drive's control software to generate the most challenging training and test trajectories possible.

B. Koopman operator approximation

Koopman operator identification for a single motor drive is now considered. Lifting functions for the motor drive are chosen based on the nonlinear oscillations that are known to be present in Harmonic Drive gearboxes [8], [9]. This oscillation is kinematic in nature [8], [9] with a fixed phase, which can be treated as a calibration parameter that must be identified for each motor drive. EDMD is then used to identify the Koopman matrix given the calibrated lifting functions.

1) *Lifting function selection*: Harmonic Drive gearboxes are known to generate vibrations at a frequency once and twice the input frequency [8], [9]. These oscillations are first characterized experimentally, and then used to inform the design of Koopman lifting functions.

Let $\theta(t)$ be the gearbox output angle in rad and let $i(t)$ be the measured motor current as a fraction of the full-scale current. The nonlinear vibration can be modelled as an exogenous load torque disturbance, which is proportional to the current disturbance [9]

$$i^d(t) = a_1 \sin(r\theta(t) + \varphi_1) + a_2 \sin(2r\theta(t) + \varphi_2), \quad (34)$$

where a_1 and a_2 are vibration amplitudes, φ_1 and φ_2 are phase shifts, and r is the reduction ratio of the gearbox. These vibrations appear as tracking errors in the position and velocity of the drive. They also appear in the current command due to the feedback action of the controller. Figure 4 shows the power spectral density of a drive's velocity tracking error during a constant 0.5 rev/s movement, which is the drive's maximum speed. Since the gearbox reduction ratio is known

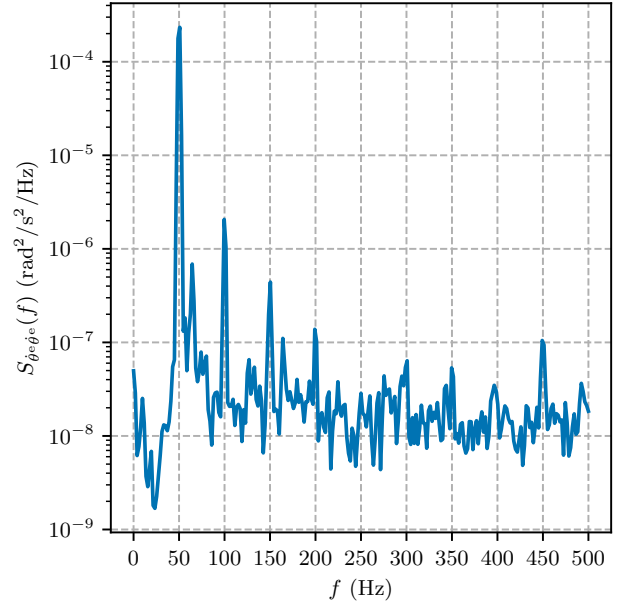


Fig. 4: Power spectral density of output velocity tracking error during a constant-velocity trajectory segment. The velocity at the gearbox input is 50 rev/s, leading to vibrations at integer multiples of 50 Hz. The most prominent tracking errors occur at the fundamental frequency. A logarithmic scale is used to better show the high-frequency harmonics.

to be $r = 100$, the resulting gearbox input velocity is 50 rev/s. Velocity tracking errors occur at integer multiples of 50 Hz, with decreasing power as frequency increases. By several orders of magnitude, the most significant tracking errors occur at 50 Hz.

Inspired by Figure 4 and by (34), the Koopman lifting functions for the motor drive system are chosen to be

$$\boldsymbol{\vartheta}_k = \begin{bmatrix} \theta_k \\ \dot{\theta}_k \\ \sin(100\theta_k + \varphi) \end{bmatrix}, \quad (35)$$

$$\mathbf{v}_k = i_k. \quad (36)$$

Since the 50 Hz error in Figure 4 is by far the largest, only that sinusoidal term is included in the lifting functions. It was found experimentally that including higher-frequency harmonics has a minimal effect on the system's overall prediction error. The vibration amplitude a_1 is identified as part of the approximated Koopman matrix. Note the inclusion of a constant phase offset φ in (35), which must be computed for each drive. A simple calibration procedure for φ is discussed in Appendix B.

2) *Koopman regression*: EDMD with Tikhonov regularization [63] is used to identify Koopman matrices using linear lifting functions and the lifting functions (35) and (36). A manual bisection procedure is used to find the smallest regularization coefficient that results in stable Koopman systems for each drive, both with linear and nonlinear lifting functions. The Tikhonov regularization coefficient required to stabilize all Koopman models is $\alpha = 90$. More advanced methods like those in [64] could also be used to guarantee asymptotic sta-

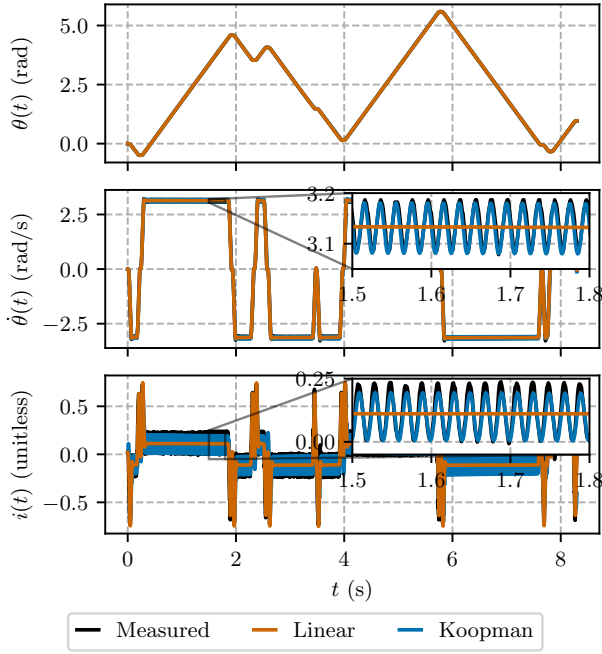


Fig. 5: Predicted position, velocity, and current trajectories for linear and Koopman drive models using the first test episode. The linear model is not able to reproduce the Harmonic Drive oscillations, and instead predicts the average velocity and current. The Koopman model is able to accurately predict the oscillations.

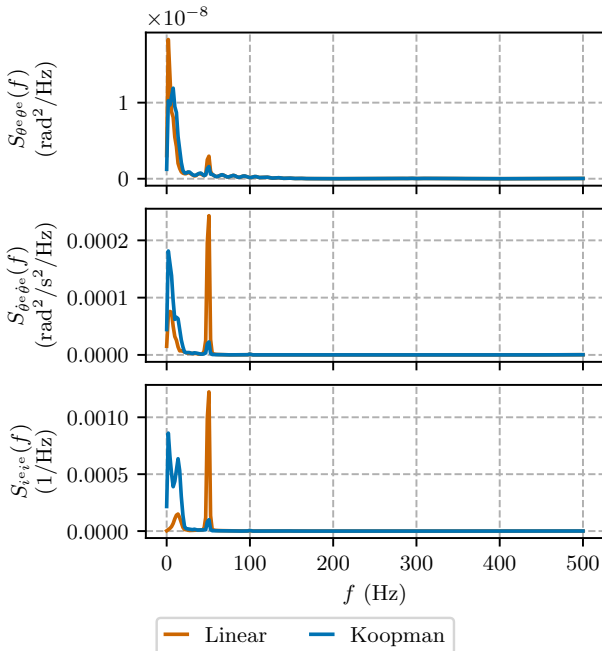


Fig. 6: Predicted position, velocity, and current error power spectral densities for linear and Koopman drive models using the first test episode. The Koopman model better predicts the gearbox oscillations, leading to lower velocity and current errors at 50 Hz. A linear scale is used to emphasize the difference in error.

bility without such a high regularization coefficient. However, in spite of the large regularization coefficient, the identified models are shown to result in good predictive performance and observer designs.

3) *Prediction results:* The predicted position, velocity, and current trajectories of one motor drive are shown in Figure 5. The corresponding prediction errors are shown in Figure 6 in the frequency domain. Figure 5 shows that the linear model correctly identifies the low-frequency dynamics of the motor drive, but does not predict the vibrations induced by the Harmonic Drive gearbox. In contrast, the Koopman model predicts the oscillations accurately. Figure 6 shows the power spectral density of the prediction errors, which demonstrate that the Koopman model significantly reduces prediction errors at 50 Hz, while introducing more low-frequency current prediction error. While higher accuracy could be obtained by using a more complex Koopman model, the simplicity of the proposed model is advantageous because it will lead to a lower-order observer design.

C. Uncertainty characterization

Now that a Koopman model for each motor drive has been identified, uncertainty is quantified within the population. Rather than computing an average model to use as the nominal plant, one motor drive model from the population is chosen as the nominal plant. For each uncertainty form and for each choice of nominal plant, residual transfer matrices are computed. The uncertainty form and nominal plant yielding the lowest peak residual is selected for observer design. For the sake of comparison, the same nominal plant is used for the linear and Koopman approaches, selected using the Koopman model's residuals.

Figure 7 shows the upper bounds on the maximum singular values of the residuals for each uncertainty form. For each uncertainty form, the nominal plant yielding the lowest uncertainty is shown. Both output multiplicative uncertainty forms have high gain over the whole frequency spectrum, and are therefore unsuitable for controller or observer design. The input multiplicative uncertainty forms are more desirable, as they have low uncertainty at low frequency and their gains remain below 0 dB over all frequencies. Between the two, the inverse input multiplicative uncertainty form has the lowest gain at high frequencies, so it is selected for observer design.

The linear inverse input multiplicative uncertainty bound in Figure 7 has lower uncertainty than the Koopman uncertainty bound at low frequencies, but similar uncertainty at high frequencies. Both uncertainty bounds have sufficiently low uncertainty for controller or observer design at low frequencies.

The uncertainty bounds in Figure 7 are computed frequency-by-frequency. Once an uncertainty model is selected, transfer functions must be designed to bound them. A nonlinear optimization problem is solved to find the transfer function coefficients that result in a magnitude response that closely bounds the residuals at each frequency. Figure 8 shows the uncertainty weights bounding the linear and Koopman residuals. Individual weighting functions are computed for each input-to-output transfer function. For the linear model, first- and

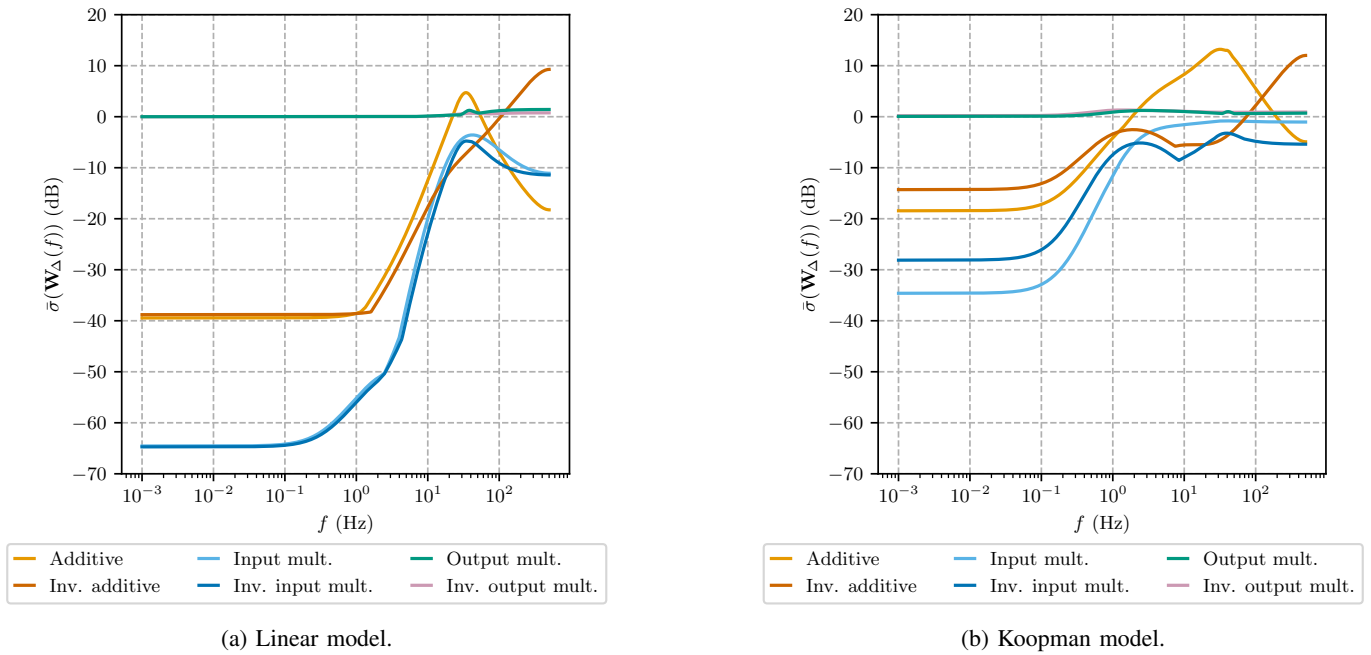


Fig. 7: Upper bounds on the residuals for each uncertainty form. Both output multiplicative uncertainty forms have high uncertainty everywhere, while both input multiplicative forms have uncertainty below 0 dB everywhere. Inverse input multiplicative uncertainty is preferred, as it remains lower than its feedforward counterpart at higher frequencies.

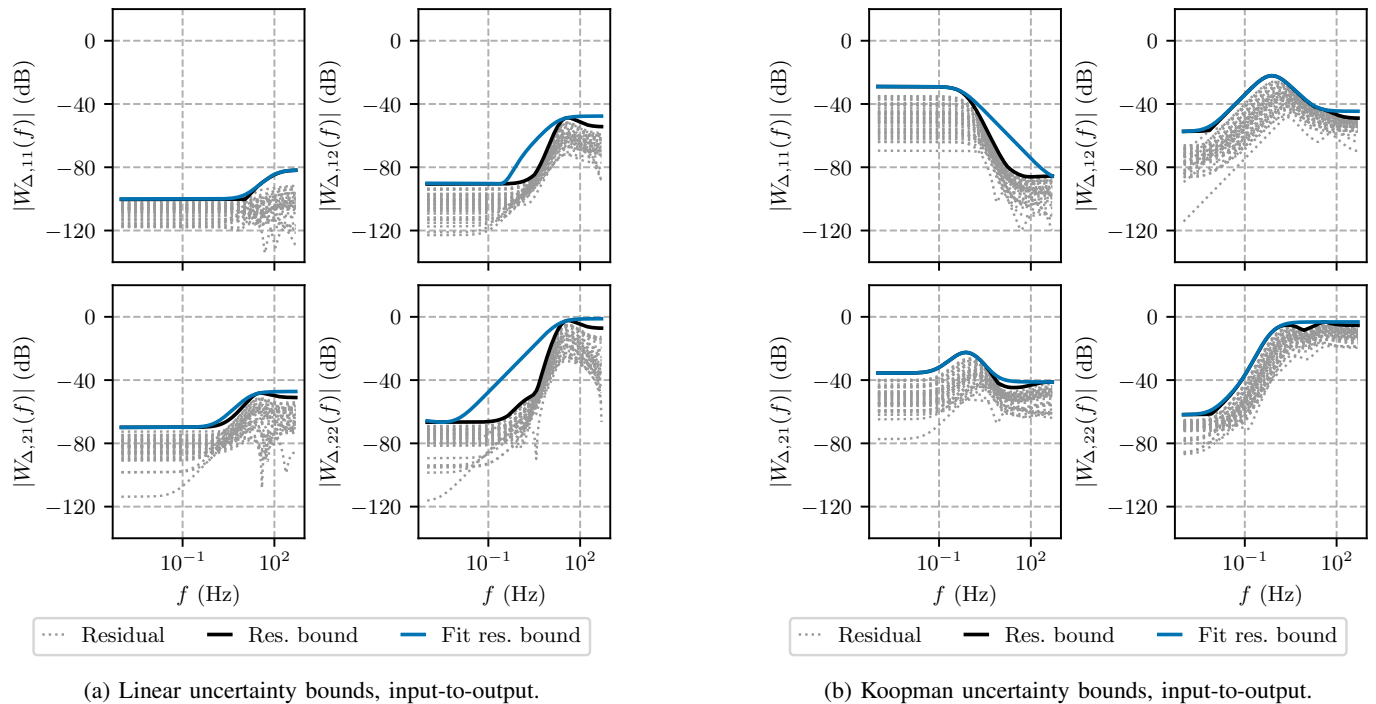


Fig. 8: Inverse input multiplicative uncertainty bounds and fit transfer functions for linear and Koopman models.

second-order transfer functions are used. The Koopman models require third-order transfer functions, except for $W_{\Delta,11}(z)$, which uses a first-order transfer function. In both the linear and Koopman cases, $W_{\Delta,22}(z)$ represents the majority of the uncertainty in the transfer matrix. While the linear and Koopman uncertainty bounds have similar magnitudes at high frequencies, the Koopman uncertainty bound is easier to fit closely with a low-order transfer function.

D. Robust observer design

Robust observers are now synthesized for both linear and Koopman models of the motor drive population. Since the motor drive has no true velocity sensor, motor velocity and current are observed given position measurements. Because the observer is synthesized using unloaded models, the motor current can be viewed as a proxy for the motor's electromagnetic torque. When the observer is fed measurements from a loaded drive, it predicts only the electromagnetic torque, not the load torque. Consequently, the current prediction error can be viewed as an estimate of the motor drive's load torque.

1) *Observer generalized plant*: The generalized plant used for robust observer synthesis, depicted in Figure 9, is inspired by the input-output observer originally proposed in [11], [38]. The controller component of the observer, \mathcal{K} is synthesized by

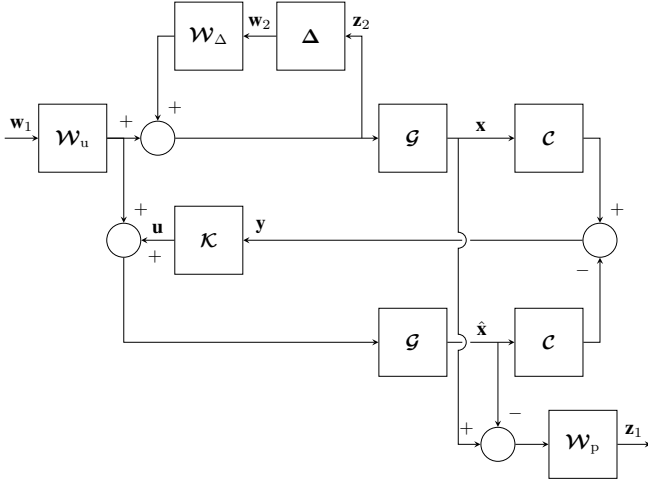


Fig. 9: The generalized plant for a robust input-output observer problem with inverse input multiplicative uncertainty.

solving a mixed \mathcal{H}_2 - \mathcal{H}_∞ robust control problem. The \mathcal{H}_2 norm is a suitable performance metric for an observer due to its interpretation as the expected RMS output of a system subject to unit variance white noise input [2, §3.3.3] [3, §5.7] [43]. Recall (22) and let the states and state-space matrices of \mathcal{W}_p , \mathcal{W}_u , and \mathcal{W}_Δ be denoted similarly with superscripts.

A state-space realization of the generalized plant is

$$\begin{bmatrix} \mathbf{x}_{k+1} \\ \hat{\mathbf{x}}_{k+1} \\ \mathbf{x}_{k+1}^{\mathcal{W}_p} \\ \mathbf{x}_{k+1}^{\mathcal{W}_u} \\ \mathbf{x}_{k+1}^{\mathcal{W}_\Delta} \end{bmatrix} = \begin{bmatrix} \mathbf{A} & \mathbf{0} & \mathbf{0} & \mathbf{BC}^{\mathcal{W}_u} & \mathbf{BC}^{\mathcal{W}_\Delta} \\ \mathbf{0} & \mathbf{A} & \mathbf{0} & \mathbf{BC}^{\mathcal{W}_u} & \mathbf{0} \\ \mathbf{B}^{\mathcal{W}_p} & -\mathbf{B}^{\mathcal{W}_p} & \mathbf{A}^{\mathcal{W}_p} & \mathbf{0} & \mathbf{0} \\ \mathbf{0} & \mathbf{0} & \mathbf{0} & \mathbf{A}^{\mathcal{W}_u} & \mathbf{0} \\ \mathbf{0} & \mathbf{0} & \mathbf{0} & \mathbf{0} & \mathbf{A}^{\mathcal{W}_\Delta} \end{bmatrix} \begin{bmatrix} \mathbf{x}_k \\ \hat{\mathbf{x}}_k \\ \mathbf{x}_k^{\mathcal{W}_p} \\ \mathbf{x}_k^{\mathcal{W}_u} \\ \mathbf{x}_k^{\mathcal{W}_\Delta} \end{bmatrix} + \begin{bmatrix} \mathbf{BD}^{\mathcal{W}_u} & \mathbf{BD}^{\mathcal{W}_\Delta} \\ \mathbf{BD}^{\mathcal{W}_u} & \mathbf{0} \\ \mathbf{0} & \mathbf{0} \\ \mathbf{B}^{\mathcal{W}_u} & \mathbf{0} \\ \mathbf{0} & \mathbf{B}^{\mathcal{W}_\Delta} \end{bmatrix} \begin{bmatrix} \mathbf{w}_{1,k} \\ \mathbf{w}_{2,k} \end{bmatrix} + \begin{bmatrix} \mathbf{0} \\ \mathbf{B} \\ \mathbf{0} \\ \mathbf{0} \\ \mathbf{0} \end{bmatrix} \mathbf{u}_k, \quad (37)$$

$$\begin{bmatrix} \mathbf{z}_{1,k} \\ \mathbf{z}_{2,k} \end{bmatrix} = \begin{bmatrix} \mathbf{D}^{\mathcal{W}_p} & -\mathbf{D}^{\mathcal{W}_p} & \mathbf{C}^{\mathcal{W}_p} & \mathbf{0} & \mathbf{0} \\ \mathbf{0} & \mathbf{0} & \mathbf{0} & \mathbf{C}^{\mathcal{W}_u} & \mathbf{C}^{\mathcal{W}_\Delta} \end{bmatrix} \begin{bmatrix} \mathbf{x}_k \\ \hat{\mathbf{x}}_k \\ \mathbf{x}_k^{\mathcal{W}_p} \\ \mathbf{x}_k^{\mathcal{W}_u} \\ \mathbf{x}_k^{\mathcal{W}_\Delta} \end{bmatrix} + \begin{bmatrix} \mathbf{0} & \mathbf{0} \\ \mathbf{D}^{\mathcal{W}_u} & \mathbf{D}^{\mathcal{W}_\Delta} \end{bmatrix} \begin{bmatrix} \mathbf{w}_{1,k} \\ \mathbf{w}_{2,k} \end{bmatrix} + \begin{bmatrix} \mathbf{0} \\ \mathbf{0} \end{bmatrix} \mathbf{u}_k, \quad (38)$$

$$\mathbf{y}_k = \begin{bmatrix} \mathbf{C} & -\mathbf{C} & \mathbf{0} & \mathbf{0} & \mathbf{0} \end{bmatrix} \begin{bmatrix} \mathbf{x}_k \\ \hat{\mathbf{x}}_k \\ \mathbf{x}_k^{\mathcal{W}_p} \\ \mathbf{x}_k^{\mathcal{W}_u} \\ \mathbf{x}_k^{\mathcal{W}_\Delta} \end{bmatrix} + \begin{bmatrix} \mathbf{0} & \mathbf{0} \end{bmatrix} \begin{bmatrix} \mathbf{w}_{1,k} \\ \mathbf{w}_{2,k} \end{bmatrix} + \mathbf{0} \mathbf{u}_k. \quad (39)$$

Using these state-space matrices, an \mathcal{H}_2 - \mathcal{H}_∞ optimal controller is synthesized using the approach of [40, §5.4.4]. The final observer has the structure shown in Figure 2.

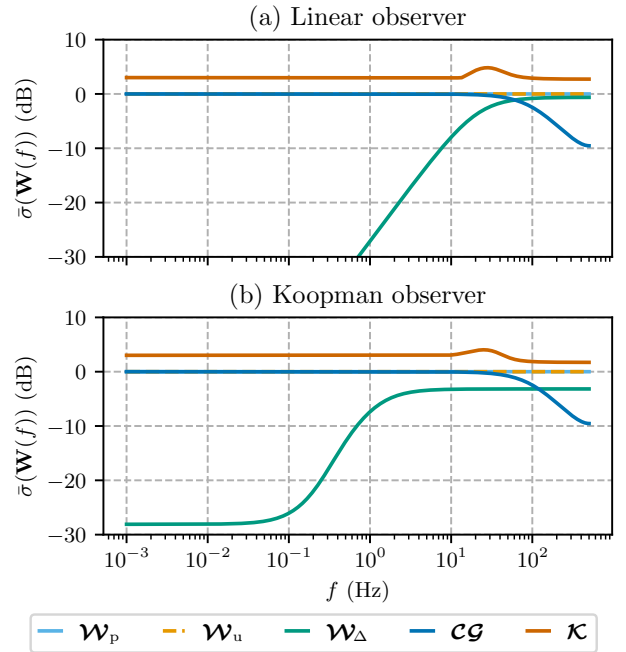


Fig. 10: Performance, input, and uncertainty weights for the linear (a) and Koopman (b) observer, along with the plant and controller frequency responses. The linear uncertainty weight is close to 0 dB above 100 Hz, leading to higher controller gains and degraded performance at high frequencies.

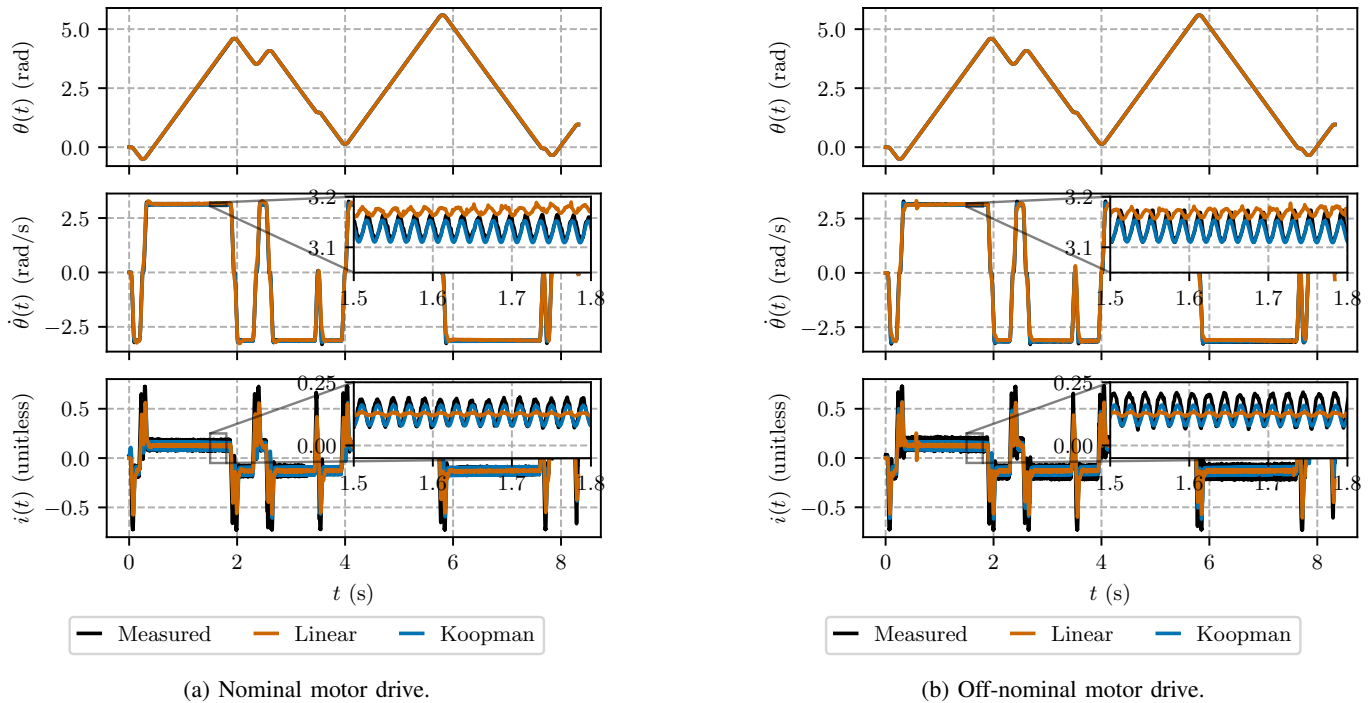


Fig. 11: Estimated position, velocity, and current trajectories of the linear and Koopman observers for the nominal and the worst off-nominal systems. The Koopman observer is able to accurately predict the Harmonic Drive oscillations while the linear observer is not. In fact, the linear model's transient velocity estimates are degraded due to higher model uncertainty at high frequencies. Off-nominal predictions are slightly worse for all observers.

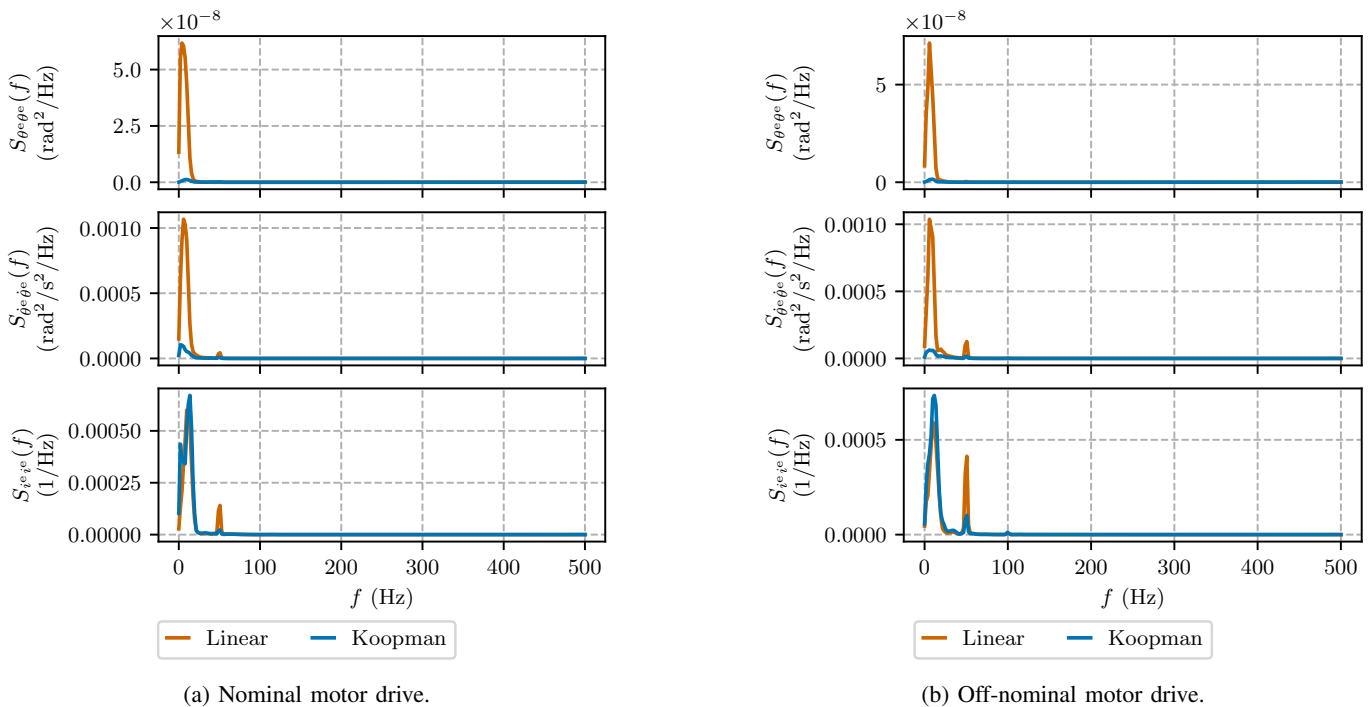


Fig. 12: Power spectral densities of position, velocity, and current estimation errors of the linear and Koopman observers for the nominal and worst off-nominal systems. In both cases, the Koopman observer reduces state estimation errors at 50 Hz. A linear scale is used to emphasize the difference in error.

The observer synthesis procedure is identical for the linear and Koopman models, as they are both represented by state-space matrices. When using the Koopman model for prediction in the Koopman observer, the original system states are recovered and re-lifted with new exogenous inputs at each timestep.

2) *Observer weighting functions*: Figure 10 shows the specific weighting functions used in the robust observer synthesis problem. The generalized plant has one performance input and one performance output: \mathbf{w}_1 , which is the weighted system input, and \mathbf{z}_1 , which is the weighted state estimation error. For the sake of comparison, the input and performance weights are left as identity. In the Koopman observer, the performance weight for the lifted state estimation error is zero. Only the uncertainty weight differs between the linear and Koopman observer synthesis problems.

The intuition for how the observer weight affects the performance of the observer is as follows. The controller component of the observer, \mathcal{K} , governs the degree to which the observer's internal nominal plant model is corrected. Low uncertainty indicates that the true plant and nominal plant match well, so the predictions of the observer's internal plant model should be trusted, and its input should not be corrected. This corresponds to a low controller gain. High uncertainty indicates that the true plant and the nominal plant may differ significantly, so measurements should be used to correct the observer's internal nominal plant model. This corresponds to a high controller gain. In Figure 10, the controller gain rises as the model uncertainty rises. As the plant gain rolls off, so does the controller gain. The linear model has higher uncertainty at high frequencies, so the controller gain remains higher than that of the Koopman model. In the next section, this effect is shown to degrade state estimation performance.

E. Experimental results

The performance of the linear and Koopman robust observers is compared in this section. Three test conditions are considered. First, the observers are tested with measurements from their nominal motor drive. Then they are tested with measurements from the furthest off-nominal motor drive. Finally, the observers are tested with measurements from the loaded nominal motor drive.

1) *Performance with nominal and off-nominal drives*: The linear and Koopman observers are now compared for both the nominal motor drive and the worst off-nominal motor drive. The worst off-nominal motor drive is the motor drive with the largest residual in Figure 8. Figure 11 shows the position, velocity, and current state estimates for the nominal and off-nominal motor drives. In both cases, the Koopman observer is able to account for the gearbox oscillation while the linear model is not. Due to higher model uncertainty at high frequencies, the linear observer's transient velocity predictions are less accurate than those of the Koopman observer. There is a slight performance decrease going from the nominal to the off-nominal motor drive, but the performance is still acceptable. Figure 12 shows the corresponding state estimation errors in the frequency domain. The Koopman observer significantly reduces errors at 50 Hz.

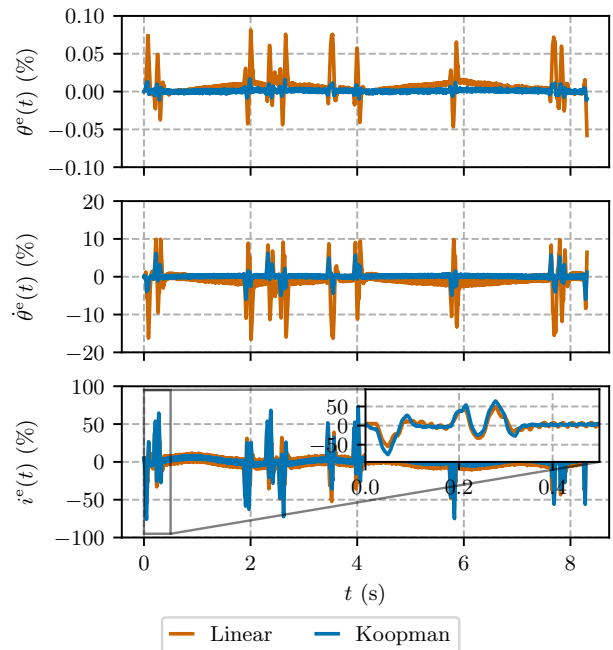


Fig. 13: Position, velocity, and current estimation errors for linear and Koopman observers for the nominal plant with an asymmetric inertial load. The current estimation error $i^e(t)$ can be treated as an estimate of the load torque. The Koopman observer's load torque estimate is less affected by Harmonic Drive gearbox oscillations.

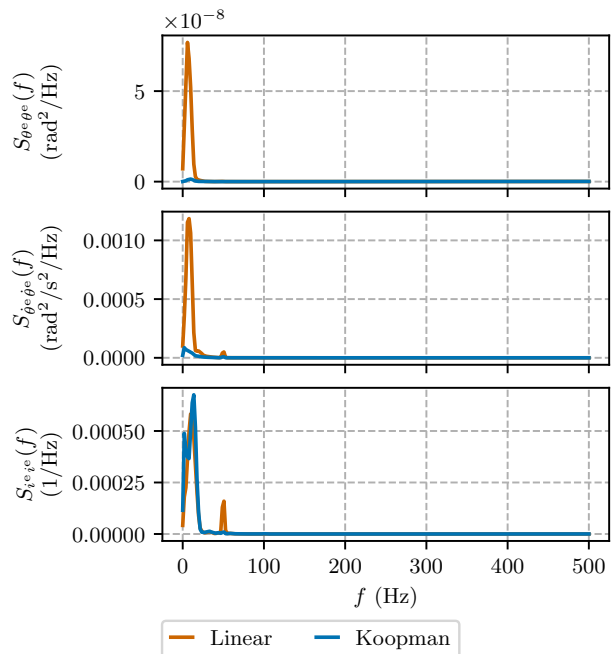
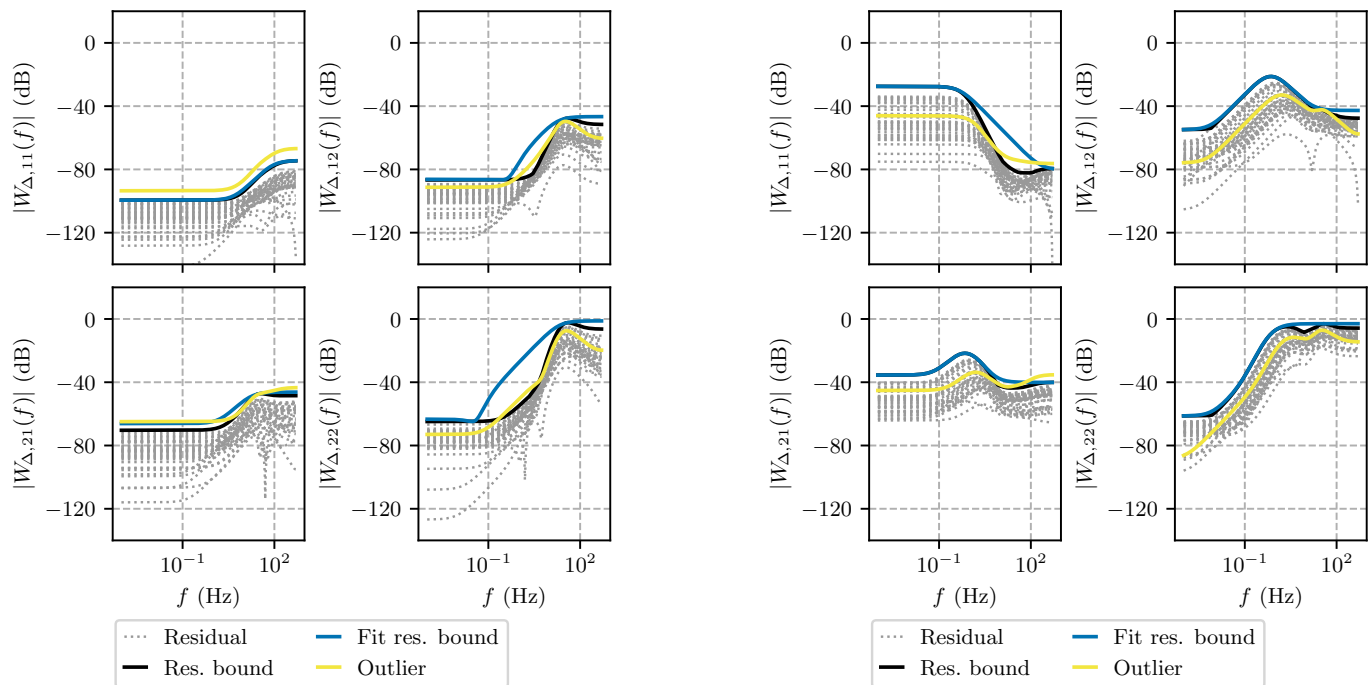


Fig. 14: Power spectral densities of position, velocity, and current estimation errors for linear and Koopman observers for the nominal plant with an asymmetric inertial load. The Koopman observer's load torque estimate is less affected by the 50 Hz Harmonic Drive gearbox oscillations.



(a) Linear uncertainty bounds and outliers, input-to-output.

(b) Koopman uncertainty bounds and outliers, input-to-output.

Fig. 15: Inverse input multiplicative uncertainty bounds, fit transfer functions, and outlier residual for linear and Koopman models. The outlier residual exceeds the fit residual bound in $W_{\Delta,11}(f)$ and $W_{\Delta,21}(f)$ in both cases.

2) *Performance with loaded drive*: Observer performance is now assessed for the nominal motor drive with an asymmetric inertial load attached. Due to the force of gravity, the load introduces a low-frequency sinusoidal disturbance to the system. The goal of the observer in this context is to estimate the low-frequency load disturbance while rejecting the high-frequency gearbox disturbance.

Since the linear and Koopman models were not identified using loaded data, the current prediction errors of their corresponding observers can be treated as estimates of the external load torque on the motor drive, particularly when angular acceleration is low. The state estimation errors of these observers are shown in Figure 13, where $i^e(t)$ can be treated as a load torque estimate. Figure 14, which contains the power spectral densities of the state estimation errors, shows that the Koopman load torque estimate contains less 50 Hz Harmonic Drive disturbance than the linear load estimate.

V. CONCLUSION

This paper proposes a robust nonlinear observer synthesis method based on the Koopman operator. Thanks to the linearity of the Koopman operator, uncertainty within a population of Koopman models can be quantified in the frequency domain, which allows standard robust controller synthesis tools to be used to synthesize a nonlinear observer. The proposed methodology is general enough that it can be applied to any system that can be modelled with the Koopman operator.

A detailed and industrially relevant experimental example is also presented, wherein Koopman models for a population of 38 motor drives are identified and uncertainty within the

population is quantified using standard robust control tools. The corresponding dataset is publicly available at [39]. Using this uncertainty model, a mixed \mathcal{H}_2 - \mathcal{H}_∞ robust observer is designed to estimate motor velocity and current from position measurements. While much contemporary Koopman control literature focuses on simulated systems, the proposed observer design approach is demonstrated with real data. Furthermore, the state-of-the-art in robust Koopman control considers only very simple uncertainty models compared to those presented here.

As with many Koopman control approaches, one limiting factor in this approach is that it does not lift the control inputs in the Koopman model. Bilinear lifting approaches like [65] show great potential for MPC algorithms, but may be difficult to integrate with LTI controllers. The proposed observer design approach can equally be used to synthesize robust optimal controllers, which is a topic that will be explored in future work.

ACKNOWLEDGMENTS

The authors thank Martin Dionne, Eric Boutet, and Jonathan Coulombe for their assistance in collecting the motor drive dataset used in this paper. The authors also thank Alexandre Coulombe for providing a photo of the motor drive used in this paper and Jonathan Eid for providing an implementation of the optimization algorithm used to fit bounds to transfer function residuals.

APPENDIX A OUTLIER DETECTION

If a motor drive is installed in its frame with inappropriate fastener torques, tracking performance is degraded and oscillations induced by the Harmonic Drive gearbox are worsened. This effect is most apparent when the motor drive is loaded. The uncertainty characterization approach described in Section IV can be used to identify motor drives that do not belong to the training population, including motor drives that are installed incorrectly.

The uncertainty characterization procedure is now repeated for the loaded dataset, using the same optimization procedure to determine weighting functions. The inverse input multiplicative residuals corresponding to a motor drive that was deliberately installed with incorrect fastener torques are shown in Figure 15. The incorrectly installed motor drive can be identified by looking at $W_{\Delta,11}(f)$ in Figure 15a and $W_{\Delta,21}(f)$ in Figure 15b, where the outlier residuals exceed the fit residual bound.

While inverse input multiplicative uncertainty is shown in this section, the outlier drive is detectable using any uncertainty model. It has been verified that this outlier identification criterion is insensitive to the choice of nominal model. All choices of nominal model except one correctly identify the outlier model. It could be argued that that nominal model should also be considered an outlier. Ultimately, the decision of whether a system should be considered an inlier or outlier depends on the use case. The uncertainty mode could equally be extended to include the incorrectly installed drive if a more conservative uncertainty model is acceptable.

APPENDIX B HARMONIC DRIVE PHASE CALIBRATION

The Koopman lifting functions in (35) include a fixed parameter for the phase of the nonlinear oscillation term, which must be determined before computing the Koopman matrix. Since this parameter is determined when the motor drive is being assembled, it is unknown but constant. This section proposes a calibration procedure for this unknown phase offset that can easily be incorporated into the motor drive's existing calibration routine.

Designing lifting functions to include both $\cos(100\theta_k)$ and $\sin(100\theta_k)$ could account for an unknown phase offset by absorbing it into the Koopman matrix. While this may be appropriate when identifying a single motor drive, it significantly and artificially increases uncertainty within a population of motor drives, negatively impacting observer performance. In an earlier version of this work, the phase offset is determined through a hyperparameter optimization procedure [66]. However, a simpler and more reliable method is presented in this paper.

To find the phase offset for a given drive, the position and velocity trajectories are separated into constant-velocity segments. For each segment i , the velocity tracking error θ_i^e is calculated and normalized, and the optimum phase,

$$\varphi_i = \arg \max_{\hat{\varphi}_i} \left\langle \hat{\theta}_i^e, \sin(100\theta_i + \hat{\varphi}_i) \right\rangle, \quad (40)$$

is found by evaluating 1000 phase samples in $[0, 2\pi)$. The final phase offset is then calculated by averaging the optimal phase of each segment using the circular mean [67, §2.2.1],

$$\varphi = \text{atan2} \left(\frac{1}{N} \sum_{i=1}^N \sin \varphi_i, \frac{1}{N} \sum_{i=1}^N \cos \varphi_i \right), \quad (41)$$

where N is the number of segments. To avoid this offline calibration procedure, a phase-locked loop could be used to estimate φ online from velocity tracking errors.

REFERENCES

- [1] S. Skogestad and I. Postlethwaite, *Multivariable Feedback Control: Analysis and Design*. West Sussex, England: Wiley, 2006.
- [2] M. Green and D. J. N. Limebeer, *Linear Robust Control*. London, England: Prentice Hall, 1994.
- [3] K. Zhou, J. C. Doyle, and K. Glover, *Robust and Optimal Control*. Englewood Cliffs, NJ: Prentice Hall, 1995.
- [4] B. O. Koopman, "Hamiltonian systems and transformations in Hilbert space," *Proc. Nat. Acad. Sci.*, vol. 17, no. 5, pp. 315–318, 1931.
- [5] I. Mezić, "Spectrum of the Koopman operator, spectral expansions in functional spaces, and state-space geometry," *J. Nonlinear Sci.*, vol. 30, no. 5, pp. 2091–2145, 2019.
- [6] M. Budišić, R. Mohr, and I. Mezić, "Applied Koopmanism," *Chaos*, vol. 22, no. 4, 2012.
- [7] A. Mauroy, I. Mezić, and Y. Susuki, Eds., *The Koopman Operator in Systems and Control*. Cham, Switzerland: Springer, 2020.
- [8] F. H. Ghorbel, P. S. Gandhi, and F. Alpeter, "On the kinematic error in harmonic drive gears," *J. Mech. Des.*, vol. 123, no. 1, pp. 90–97, 1998.
- [9] T. Tuttle and W. Seering, "A nonlinear model of a harmonic drive gear transmission," *IEEE Trans. Robot. Autom.*, vol. 12, no. 3, pp. 368–374, 1996.
- [10] Z. Wang and H. Unbehauen, "A class of nonlinear observers for discrete-time systems with parametric uncertainty," *Int. J. Syst. Sci.*, vol. 31, no. 1, pp. 19–26, 2000.
- [11] H. Marquez and M. Riaz, "Robust state observer design with application to an industrial boiler system," *Control Eng. Pract.*, vol. 13, no. 6, pp. 713–728, 2005.
- [12] L. Etienne, K. A. Langueh, H. Karkaba, and A. Iovine, "Robust observer synthesis for bilinear parameter varying system," in *Proc. 61st Conf. Decis. Control*. IEEE, 2022, pp. 1900–1905.
- [13] G. Lu and D. Ho, "Robust \mathcal{H}_∞ observer for nonlinear discrete systems with time delay and parameter uncertainties," *IEE Proc. — Control Theory Appl.*, vol. 151, no. 4, pp. 439–444, 2004.
- [14] A. M. Pertew, H. J. Marquez, and Q. Zhao, " \mathcal{H}_∞ synthesis of unknown input observers for non-linear Lipschitz systems," *Int. J. Control*, vol. 78, no. 15, pp. 1155–1165, 2005.
- [15] M. Abbaszadeh and H. J. Marquez, "Robust \mathcal{H}_∞ observer design for sampled-data Lipschitz nonlinear systems with exact and Euler approximate models," *Automatica*, vol. 44, no. 3, pp. 799–806, 2008.
- [16] —, "LMI optimization approach to robust \mathcal{H}_∞ observer design and static output feedback stabilization for discrete-time nonlinear uncertain systems," *Int. J. Robust Nonlinear Control*, vol. 19, no. 3, pp. 313–340, 2008.
- [17] R. Raoufi, H. J. Marquez, and A. S. I. Zinober, " \mathcal{H}_∞ sliding mode observers for uncertain nonlinear Lipschitz systems with fault estimation synthesis," *Int. J. Robust Nonlinear Control*, vol. 20, no. 16, pp. 1785–1801, 2010.
- [18] A. Surana, "Koopman operator based observer synthesis for control-affine nonlinear systems," in *Proc. 55th IEEE Conf. Decis. Control*. IEEE, 2016.
- [19] A. Surana and A. Banaszuk, "Linear observer synthesis for nonlinear systems using Koopman operator framework," *IFAC-PapersOnLine*, vol. 49, no. 18, pp. 716–723, 2016.
- [20] D. F. Gomez, F. D. Lagor, P. B. Kirk, A. H. Lind, A. R. Jones, and D. A. Paley, "Data-driven estimation of the unsteady flowfield near an actuated airfoil," *J. Guid. Control Dyn.*, vol. 42, no. 10, pp. 2279–2287, 2019.
- [21] M. Netto and L. Mili, "A robust data-driven Koopman Kalman filter for power systems dynamic state estimation," *IEEE Trans. Power Syst.*, vol. 33, no. 6, pp. 7228–7237, 2018.
- [22] J. D. Lee, S. Im, L. Kim, H. Ahn, and H. Bang, "Data-driven fault detection and isolation for multirotor system using Koopman operator," *J. Intell. Robot. Syst.*, vol. 110, no. 3, 2024.

- [23] A. Lambe and S. N. Sharma, "On embedding the Koopmanization into controlled nonlinear systems , its comparison with the Carleman linearisation and concerning results: beyond the feedback linearisation," *Int. J. Syst. Sci.*, pp. 1–21, 2024.
- [24] Z. C. Guo, V. Korotkine, J. R. Forbes, and T. D. Barfoot, "Koopman linearization for data-driven batch state estimation of control-affine systems," *IEEE Robot. Autom. Lett.*, vol. 7, no. 2, pp. 866–873, 2022.
- [25] Z. C. Guo, F. Dümbs, J. R. Forbes, and T. D. Barfoot, "Data-driven batch localization and SLAM using Koopman linearization," *IEEE Trans. Robot.*, vol. 40, pp. 3964–3983, 2024.
- [26] D. Uchida, A. Yamashita, and H. Asama, "Data-driven Koopman controller synthesis based on the extended \mathcal{H}_2 norm characterization," *IEEE Contr. Syst. Lett.*, vol. 5, no. 5, pp. 1795–1800, 2021.
- [27] R. Strässer, J. Berberich, and F. Allgöwer, "Robust data-driven control for nonlinear systems using the Koopman operator," *IFAC-PapersOnLine*, vol. 56, no. 2, pp. 2257–2262, 2023.
- [28] R. Strässer, M. Schaller, K. Wörthmann, J. Berberich, and F. Allgöwer, "Koopman-based feedback design with stability guarantees," *IEEE Trans. Autom. Control*, pp. 1–16, 2024.
- [29] T. He and A. Pal, "Dual-loop robust control of biased Koopman operator model by noisy data of nonlinear systems," [arXiv:2401.08536v2 \[eess.SY\]](https://arxiv.org/abs/2401.08536v2), 2024.
- [30] M. Eyüboğlu, N. Powell, and A. Karimi, "Data-driven control synthesis using Koopman operator: A robust approach," in *Proc. 2024 Am. Control Conf.*, Toronto, Canada, 2024.
- [31] F. Ganz, A. Datar, P. Gottsch, and H. Werner, "Data-driven \mathcal{H}_∞ optimal controller design using the Koopman operator: Case study," in *Proc. 2021 Eur. Control Conf.* IEEE, 2021.
- [32] S. L. Brunton, M. Budišić, E. Kaiser, and J. N. Kutz, "Modern Koopman theory for dynamical systems," *SIAM Review*, vol. 64, no. 2, pp. 229–340, 2022.
- [33] S. E. Otto and C. W. Rowley, "Koopman operators for estimation and control of dynamical systems," *Annu. Rev. Control, Robot., Auton. Syst.*, vol. 4, no. 1, pp. 59–87, 2021.
- [34] G. Mamakoukas, S. Di Cairano, and A. P. Vinod, "Robust model predictive control with data-driven Koopman operators," in *Proc. 2022 Am. Control Conf.* IEEE, 2022.
- [35] X. Zhang, W. Pan, R. Scattolini, S. Yu, and X. Xu, "Robust tube-based model predictive control with Koopman operators," *Automatica*, vol. 137, p. 110114, 2022.
- [36] T. Gholaminejad and A. Khaki-Sedigh, "Stable data-driven Koopman predictive control: Concentrated solar collector field case study," *IET Control Theory Appl.*, vol. 17, no. 9, pp. 1116–1131, 2023.
- [37] T. de Jong, V. Breschi, M. Schoukens, and M. Lazar, "Koopman data-driven predictive control with robust stability and recursive feasibility guarantees," [arXiv:2405.01292v1 \[math.OC\]](https://arxiv.org/abs/2405.01292v1), 2024.
- [38] H. Marquez, "A frequency domain approach to state estimation," *J. Frankl. Inst.*, vol. 340, no. 2, pp. 147–157, 2003.
- [39] S. Dahdah and J. R. Forbes, "Quantifying manufacturing variation in motor drives," Federated Research Data Repository, 2024.
- [40] R. J. Caverly and J. R. Forbes, "LMI properties and applications in systems, stability, and control theory," [arXiv:1903.08599v4 \[cs.SY\]](https://arxiv.org/abs/1903.08599v4), 2024.
- [41] P. J. Antsaklis and A. N. Michel, *A Linear Systems Primer*. Birkhäuser, 2007.
- [42] T. Chen and B. A. Francis, *Optimal Sampled-Data Control Systems*. Springer, 1995.
- [43] A. Megretski, "Multivariable control systems: Interpretations for standard optimization setup," 2004.
- [44] I. Kaminer, P. P. Khargonekar, and M. A. Rotea, "Mixed $\mathcal{H}_2/\mathcal{H}_\infty$ control for discrete-time systems via convex optimization," *Automatica*, vol. 29, no. 1, pp. 57–70, 1993.
- [45] N. J. Kutz, S. L. Brunton, B. W. Brunton, and J. L. Proctor, *Dynamic Mode Decomposition: Data-Driven Modeling of Complex Systems*. Philadelphia, PA: SIAM, 2016.
- [46] I. Abraham and T. D. Murphey, "Active learning of dynamics for data-driven control using Koopman operators," *IEEE Trans. Robot.*, vol. 35, no. 5, pp. 1071–1083, 2019.
- [47] G. Mamakoukas, M. Castano, X. Tan, and T. Murphey, "Local Koopman operators for data-driven control of robotic systems," in *Proc. Robot.: Sci. Syst. XV*, Freiburg im Breisgau, Germany, 2019.
- [48] E. Kaiser, J. N. Kutz, and S. L. Brunton, "Data-driven discovery of Koopman eigenfunctions for control," *Mach. Learn.: Sci. Technol.*, vol. 2, no. 3, p. 035023, 2021.
- [49] D. Bruder, B. Gillespie, C. D. Remy, and R. Vasudevan, "Modeling and control of soft robots using the Koopman operator and model predictive control," in *Proc. Robot.: Sci. Syst. XV*, Freiburg im Breisgau, Germany, 2019.
- [50] I. Abraham, G. de la Torre, and T. Murphey, "Model-based control using Koopman operators," in *Proc. Robot.: Sci. Syst. XIII*, Cambridge, MA, 2017.
- [51] A. Mallen, C. A. Keller, and J. N. Kutz, "Koopman-inspired approach for identification of exogenous anomalies in nonstationary time-series data," *Mach. Learn.: Sci. Technol.*, vol. 4, no. 2, p. 025033, 2023.
- [52] Y. Susuki, K. Eto, N. Hiramatsu, and A. Ishigame, "Control of in-room temperature field via damping assignment to nonlinear Koopman mode," *IEEE Trans. Control Syst. Technol.*, vol. 32, no. 5, pp. 1569–1578, 2024.
- [53] M. Švec, Š. Ileš, and J. Matuško, "Predictive direct yaw moment control based on the Koopman operator," *IEEE Trans. Control Syst. Technol.*, vol. 31, no. 6, pp. 2912–2919, 2023.
- [54] A. M. DeGennaro and N. M. Urban, "Scalable extended dynamic mode decomposition using random kernel approximation," *SIAM J. Sci. Comput.*, vol. 41, no. 3, pp. A1482–A1499, 2019.
- [55] A. Rahimi and B. Recht, "Random features for large-scale kernel machines," in *Proc. 20th Int. Conf. Neural Inf. Process. Syst.* Curran Associates, 2007, pp. 1177–1184.
- [56] M. Korda and I. Mezić, "Linear predictors for nonlinear dynamical systems: Koopman operator meets model predictive control," *Automatica*, vol. 93, pp. 149–160, 2018.
- [57] S. Pan and K. Duraisamy, "On the structure of time-delay embedding in linear models of non-linear dynamical systems," *Chaos*, vol. 30, no. 7, 2020.
- [58] M. O. Williams, I. G. Kevrekidis, and C. W. Rowley, "A data-driven approximation of the Koopman operator: Extending dynamic mode decomposition," *J. Nonlinear Sci.*, vol. 25, no. 6, pp. 1307–1346, 2015.
- [59] G. Mamakoukas, I. Abraham, and T. D. Murphey, "Learning data-driven stable Koopman operators," [arXiv:2005.04291v1 \[cs.RO\]](https://arxiv.org/abs/2005.04291v1), 2020.
- [60] T. Gebru, J. Morgenstern, B. Vecchione, J. W. Vaughan, H. Wallach, H. D. III, and K. Crawford, "Datasheets for datasets," *Commun. ACM*, vol. 64, no. 12, pp. 86–92, 2021.
- [61] S. Dahdah and J. R. Forbes, "decargroup/pykoop v1.2.3," Zenodo, 2023.
- [62] L. Ljung, *System Identification: Theory for the User*. Prentice Hall, 1999.
- [63] A. N. Tikhonov, A. Goncharsky, V. V. Stepanov, and A. G. Yagola, *Numerical Methods for the Solution of Ill-Posed Problems*. Dordrecht, Netherlands: Springer, 1995.
- [64] S. Dahdah and J. R. Forbes, "System norm regularization methods for Koopman operator approximation," *Proc. R. Soc. A*, vol. 478, no. 2265, 2022.
- [65] D. Bruder, X. Fu, and R. Vasudevan, "Advantages of bilinear Koopman realizations for the modeling and control of systems with unknown dynamics," *IEEE Trans. Robot. Autom.*, vol. 6, no. 3, pp. 4369–4376, 2021.
- [66] S. Dahdah and J. R. Forbes, "Closed-loop Koopman operator approximation," [arXiv:2303.15318v1 \[eess.SY\]](https://arxiv.org/abs/2303.15318v1), 2023.
- [67] K. Mardia and P. E. Jupp, *Directional Statistics*. Wiley, 1999.



Steven Dahdah (Student Member, IEEE) received the B.Eng. degree in electrical engineering (Honours, Co-op) with a minor in software engineering from McGill University, Montreal QC, Canada in 2019.

He is currently a Ph.D. candidate in the Department of Mechanical Engineering at McGill university. His research interests include control systems, system identification, and machine learning.



James Richard Forbes (Member, IEEE) received the B.A.Sc. degree in mechanical engineering (Honours, Co-op) from the University of Waterloo, Waterloo ON, Canada, in 2006, and the M.A.Sc. and Ph.D. degrees in aerospace science and engineering from the University of Toronto Institute for Aerospace Studies, Toronto ON, in 2008 and 2011, respectively.

He is currently an Associate Professor and William Dawson Scholar with the Department of Mechanical Engineering, McGill University, Montreal QC, Canada. His research interests include navigation, guidance, and control of robotic systems.

Dr. Forbes is a Member of the Centre for Intelligent Machines, a Member of the Group for Research in Decision Analysis, and a Member of the Trottier Institute for Sustainability in Engineering and Design. He was the recipient of the McGill Association of Mechanical Engineers Professor of the Year Award in 2016, the Engineering Class of 1944 Outstanding Teaching Award in 2018, the Carrie M. Derick Award for Graduate Supervision and Teaching in 2020, and the Samuel and Ida Fromson Outstanding Teaching Award in Engineering in 2024. He is currently a Senior Editor for the International Journal of Robotics Research (IJRR).